Trends in Mathematics
Information Center for Mathematical Sciences
Volume 8, Number 2, December 2005, Pages 129–152

ELECTRICAL CONDUCTIVITY IMAGING USING MAGNETIC RESONANCE ELECTRICAL IMPEDANCE TOMOGRAPHY (MREIT)

JIN KEUN SEO, OHIN KWON AND EUNG JE WOO

Abstract. Magnetic Resonance Electrical Impedance Tomography (MREIT) is a new medical imaging modality providing high resolution static conductivity images based on the current injection MRI technique. MREIT was motivated to deal with the well-known severe ill-posedness of the image reconstruction problem in Electrical Impedance Tomography (EIT). In order to bypass the ill-posed nature in EIT, MREIT takes advantage of an MRI scanner as a tool to capture partial information about magnetic flux density due to internal current density. The conductivity distribution have an effect in change in internal current density pathways that are interrelated with the unknown conductivity distribution. Lately, we have made a significant progress in reconstruction algorithms in MREIT. Experimental MREIT study demonstrates that the reconstructed conductivity image distinguishes different biological tissues in terms of both their shapes and conductivity values. Reconstructed static conductivity images will allow us to obtain internal current density images for any arbitrary injection current and electrode configuration. Very recently, we also initiated a method of reconstructing anisotropic conductivity images.

1. Introduction

Magnetic Resonance Electrical Impedance Tomography (MREIT) is a new medical imaging modality providing high resolution static conductivity images based on the current injection MRI technique. MREIT was motivated to deal with the well-known severe ill-posedness of the image reconstruction problem in Electrical Impedance Tomography (EIT). In order to bypass the ill-posed nature in EIT, MREIT takes advantage of an MRI scanner as a tool to capture partial information about magnetic flux density due to internal current density.

The electrical conductivity and permittivity of a biological tissue change with cell concentration, cellular structure, molecular composition, membrane capacitance, and so on. Therefore, these properties manifest structural, functional, metabolic, and pathological conditions of the tissue providing valuable diagnostic information. Hence, cross-sectional imaging of electrical conductivity distributions within the human body has been an important research goal in medical imaging. (Barber *1984; Brown 1987; Webster 1990; Cheney 1992; Holder 1993; Metherall 1996; Boone 1997; Saulnier 2001). Cheney 1999; Saulnier 2001).*

In EIT, finding the inhomogeneous conductivity and/or permittivity distribution in a form of cross-sectional image becomes a complicated inverse problem also known as the inverse conductivity problem. In most cases, surface electrodes as many as 8 to 256 are attached in a two or three-dimensional configuration. Injecting patterns of currents through all or chosen pairs of electrodes, induced boundary voltages on all or selected electrodes are measured. The measured boundary current-voltage data set is utilized to reconstruct cross-sectional images of the conductivity and/or permittivity distribution inside the subject. It is known that most biological tissues are anisotropic in terms of their electrical properties. Throughout this chapter, however, we only consider isotropic cases since there is no solid technique yet to deal with the anisotropy in EIT.

When we inject current into a subject, the internal current pathway or the current density distribution is affected nonlinearly by the global structure of the electrical properties of the subject. Any change in the conductivity of an internal region alters the current pathway and its effect is conveyed to the corresponding change in the boundary voltage. However, these boundary measurements are very insensitive to a local change away from measuring points. For this reason, EIT suffers from the ill-posed characteristics of the corresponding inverse problem. This makes it difficult to reconstruct accurate conductivity and/or permittivity images with a high spatial resolution under realistic environments where modelling and measurement errors are unavoidable.

In practice, we can attach only a limited number of electrodes and this means that we are limited by a fixed amount of information from boundary measurements. Using a larger number of electrodes requires a more complicated instrument and cumbersome electrode attachment procedure and these are prone to increase the total amount of measurement errors in practice. With these kinds of technical restrictions, it is desirable for EIT to find clinical applications where its portability and high temporal resolution to monitor changes in electrical properties are significant merits. This kind of impedance imaging has been called the dynamic or difference imaging in EIT. In the following sections on EIT, we will describe its mathematical formulation, image reconstruction algorithms, measurement techniques, and examples of EIT images.

On the other hand, there have been strong needs for a new imaging technique capable of providing conductivity images with sufficiently high spatial resolution and accuracy. In the following section, we will discuss why we are interested in high-resolution conductivity and current density imaging beyond the practically achievable performance of EIT techniques. In order to fulfil these needs, Magnetic Resonance Electrical Impedance Tomography (MREIT) has been proposed recently.

When we inject current into a subject, it produces distributions of voltage, current density and also magnetic flux density inside the subject. The basic idea of MREIT is to utilize the information on magnetic as well as electric field induced by the injection current. While EIT is limited by the boundary measurements of current-voltage data, MREIT utilizes the internal magnetic flux density data obtained using a Magnetic Resonance Imaging (MRI) scanner.

Since the late 1990s, imaging techniques in MREIT have been advanced rapidly and now are at the stage of animal experiments. In this paper, we review these techniques and propose future directions of MREIT research for clinical applications. Before we describe technical details of MREIT, we will briefly review EIT in order to provide the rationale of pursuing MREIT research that requires an expensive MRI scanner. Then, MREIT techniques will be reviewed starting with its mathematical formulation. The formulation will be described with the technical limitations in measuring the induced magnetic flux density using an MRI scanner. Recent progress in MREIT providing conductivity and current density images with a high spatial resolution and accuracy will be presented including image reconstruction algorithms and experimental techniques.

2. Motivation

Our human body is an electrically conducting domain with an anisotropic conductivity distribution determined by the electrical property of numerous biological tissues and organs. This kind of domain is often called a volume conductor. Inside the volume conductor, we have electrical signal sources that can be modelled as current dipoles. The origin of these signals are excitable cells such as nerves and muscles. Since there are numerous nerves and muscles inside the human body, we can consider a distribution of current dipoles. The current dipole distribution changes as physiological status of organs or parts of organs including excitable cells.

We denote the domain of the volume conductor as $\Omega \in \mathbb{R}^3$ with its boundary $\partial\Omega$. The time-varying current dipole distribution is expressed as $f(\mathbf{r};t)$ where $\mathbf{r}$ is a position vector and t is time. Assuming that the time-varying anisotropic conductivity distribution is $\underline{\underline{\sigma}}(\mathbf{r};t) = \begin{pmatrix} \sigma_{11} & \sigma_{12} & \sigma_{13} \\ \sigma_{12} & \sigma_{22} & \sigma_{23} \\ \sigma_{13} & \sigma_{23} & \sigma_{33} \end{pmatrix}$, the voltage $u(\mathbf{r},t)$ produced in Ω is a solution of the following Neumann boundary value problem:

$$\begin{cases} \nabla \cdot \left[\underline{\underline{\sigma}}(\mathbf{r};t)\nabla u(\mathbf{r};t)\right] = f(\mathbf{r};t) \text{ in } \Omega \\ -\underline{\underline{\sigma}}(\mathbf{r};t)\nabla u(\mathbf{r};t)\cdot\mathbf{n} = 0 \text{ on } \partial\Omega \end{cases} \tag{1}$$

where $\mathbf{n}$ is the outward unit normal vector on $\partial\Omega$. The Neumann data is zero on the boundary since the air is regarded as an insulator. Setting a reference voltage $u(\mathbf{r}_0;t) = 0$ for $\mathbf{r}_0 \in \partial\Omega$, we can obtain a unique solution u of (1) from $\underline{\underline{\sigma}}$ and f. The current density $\mathbf{J}$ in Ω is given by

$$\mathbf{J}(\mathbf{r};t) = -\underline{\underline{\sigma}}(\mathbf{r};t)\nabla u(\mathbf{r};t) \quad \text{in } \Omega. \tag{2}$$

The current density distribution generates a magnetic field and the magnetic flux density $\mathbf{B}$ in $\mathbb{R}^3$ is determined by the Biot-Savart law as

$$\mathbf{B}(\mathbf{r};t) = \frac{\mu_0}{4\pi}\int_\Omega \mathbf{J}(\mathbf{r}';t)\times\frac{\mathbf{r}-\mathbf{r}'}{|\mathbf{r}-\mathbf{r}'|^3}dv' \tag{3}$$

for $\mathbf{r} \in \mathbb{R}^3$. From the Ampere's law, the current density $\mathbf{J}$ is also given by

$$\mathbf{J}(\mathbf{r};t) = \frac{1}{\mu_0}\nabla\times\mathbf{B}(\mathbf{r};t) \quad \text{in } \Omega. \tag{4}$$

As the signal source f and the conductivity $\underline{\underline{\sigma}}$ change with time, the equipotential lines vary. If we attach a pair of electrodes on the boundary $\partial\Omega$ as shown in figure 2(a), we can record a bio-potential signal using an amplifier. The signal provides a partial information on f and $\underline{\underline{\sigma}}$. Figure 2(b) shows a situation of measuring the generated magnetic flux density signal outside the human head using a very sensitive magnetic sensor called SQUID (superconducting quantum interference device). This bio-magnetic signal also provides an incomplete information on f and $\underline{\underline{\sigma}}$.

The primary reason for measuring these kinds of bio-electric and bio-magnetic signals is to extract useful diagnostic information about the status of tissues or organs. Since these bio-signals are non-invasively measurable at the surface or vicinity of the human body, they have been extensively used in medicine. However, if there comes a new non-invasive technology providing more direct information on the signal source f and the conductivity distribution $\underline{\underline{\sigma}}$, there will be numerous invaluable biomedical applications.

Neural activity mapping has been actively studied in Electromagnetic Source Imaging (ESI). Excitable tissues such as nerve and muscle produce endogenous current flows along with the generation of action potentials. The current flows produce electromagnetic fields and these can be measured on the surface or outside the human body by using, for example, ECG/MCG for the heart and EEG/MEG for the brain. These signals are often used to map the distribution of the endogenous current sources through an inversion process in ESI (Phillips *1997; Mosher 1999). Neural activities are the sources for these electric and magnetic signals and they are modelled as current dipoles inside the electrically conducting domain. Since a solution of the inverse problem to find a map of a distribution of current dipoles is affected by the conductivity distribution, one of the fundamental technical difficulties in ESI is the fact that we do not know the material property, that is, the conductivity distribution. Therefore, conductivity images will improve the accuracy in the solution of the inverse problem to localize signal sources when properly utilized in ESI.*

It has been also known that conductivity changes are associated with neural activity because of ion migration (Cole and Curtis 1939; Cole 1949). Cortical impedance changes have been observed with an increase of regional cerebral blood volume due to neural activity since blood has higher conductivity than cortical tissue (Rank 1963; Geddes and Baker 1967). Similar changes due to functional activity and epilepsy have been also observed in cats and rabbits, and recently in humans (Adey *1962; Van-Harreveld and Schade 1962; Aladjolova 1964; Tidswell 2001).*

Therefore, visualizing the associated conductivity changes could be a new way of mapping neural activity. In order for a conductivity image itself to be a way of expressing a map of neural activity, the image should be provided with a high spatial resolution and accuracy.

There are numerous techniques of applying electric or magnetic energy into the human body for therapeutic purposes. Examples include cardiac defibrillation,

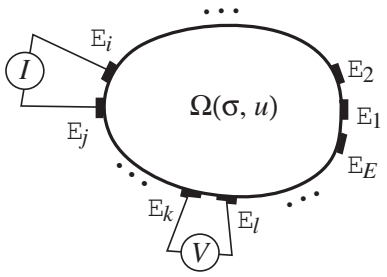

FIGURE 1. Electrically conducting subject Ω with a conductivity σ and voltage u distribution. Surface electrodes $\mathcal{E}_j, j = 1, \cdots, E$ are attached on the boundary $\partial\Omega$. Here, we assume that current is injected between the pair of electrodes $\mathcal{E}_i$ and $\mathcal{E}_j$ and voltage is measured between $\mathcal{E}_k$ and $\mathcal{E}_l$.

functional electrical stimulation, magnetic stimulation, radio-frequency ablation and others. In these cases, knowledge of tissue conductivity is necessary to determine deposition of electromagnetic energy. In general, we need to focus current density around a local region of interest to maximize the effects of the treatment. With a known conductivity distribution, one can easily determine the internal current density distribution subject to an external excitation. This will enable us to optimize the treatment methods including electrode and coil design and configuration.

3. EIT AND ITS LIMITATION

3.1. **Forward problem: voltage due to an injection current for a given conductivity.** Let $\Omega \subset \mathbb{R}^3$ be an electrically conducting subject with its boundary $\partial\Omega$ as shown in figure 1. Surface electrodes $\mathcal{E}_j$ for $j = 1, \cdots, E$ are attached on the boundary $\partial\Omega$. Assume that we inject current I through a pair of chosen electrodes. We denote a position vector in $\mathbb{R}^3$ as $\mathbf{r}$ and $\sigma(\mathbf{r})$ is a conductivity at $\mathbf{r} \in \Omega$. At a relatively low frequency range, we can define a voltage distribution u in Ω satisfying the following boundary value problem with the Neumann boundary condition:

$$\begin{cases} \nabla \cdot [\sigma(\mathbf{r})\nabla u(\mathbf{r})] = 0 \text{ in } \Omega \\ -\sigma \nabla u \cdot \mathbf{n} = g \text{ on } \partial\Omega \end{cases} \tag{5}$$

where $\mathbf{n}$ is the outward unit normal vector on $\partial\Omega$ and g the magnitude of the current density on $\partial\Omega$ due to the injection current I. On a current injection electrode $\mathcal{E}_j$, we have $\int_{\mathcal{E}_j} g\, ds = \pm I$ where ds is the surface element and the sign depends on the direction of the injection current. The Neumann data g is zero on the regions of the boundary not contacting with current injection electrodes. Setting a reference voltage $u(\mathbf{r}_0) = 0$ for $\mathbf{r}_0 \in \partial\Omega$, we can obtain a unique solution u of (5) from σ and g. The current density $\mathbf{J}$ in Ω due to the injection current is given by

$$\mathbf{J}(\mathbf{r}) = -\sigma(\mathbf{r})\nabla u(\mathbf{r}) \quad \text{in } \Omega. \tag{6}$$

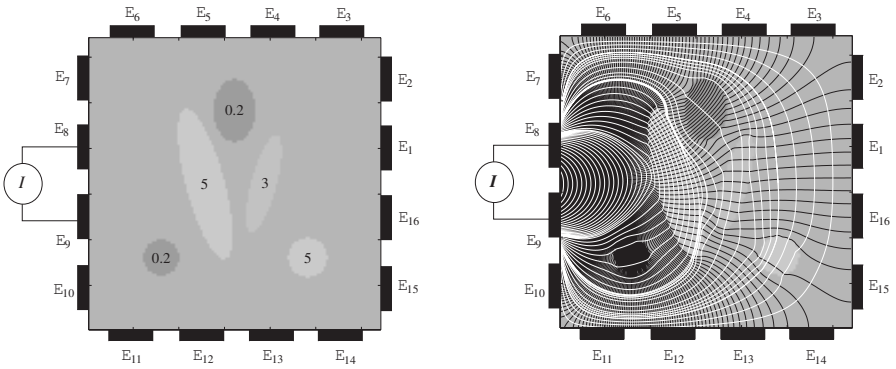

FIGURE 2. (a) An example of an electrically conducting subject with a given conductivity distribution. Numbers inside ellipsoids are conductivity values in S/m. (b) Voltage and current density distribution induced by the injection current. Black and white lines are equipotential and current density streamlines, respectively.

By EIT technique, we cannot determine an anisotropic conductivity distribution of a subject, since the boundary information of current-voltage data are not sufficient to recover the anisotropic conductivity distribution. This means that many different anisotropic conductivity distributions may have the same boundary measurements in EIT (Greenleaf *2003). For this reason, we will assume that* σ *is isotropic in this EIT section.*

Using a simple numerical example, we now illustrate how the voltage and current density distributions are formed from (5) and (6). Figure 2(a) shows a two-dimensional model of an electrically conducting subject with a given conductivity distribution σ. With sixteen electrodes on its boundary, the injection current is applied between the chosen pair of electrodes. Figure 2(b) shows the computed voltage and current density distribution using the Finite Element Method (FEM).

In EIT, we measure the boundary voltage f, the restriction of u to the boundary $\partial\Omega$, to reconstruct an image of σ. If the subject is homogeneous, a single measurement of the boundary current-voltage pair (g, f) will be enough to determine the constant σ. For the general case where the subject is inhomogeneous, the reconstruction of the target image σ requires applying several independent currents $g_j, j = 1, \cdots, N$ and measuring the corresponding boundary voltages f_j. As an example, figure 3(a) and (b) show the Neumann data g and boundary voltage f, respectively, from the model in figure 2.

Now, the inverse problem is to reconstruct σ from the boundary current-voltage pairs $(g_j, f_j), j = 1, \cdots, N$. To search for σ, it is necessary to interpret how the change in conductivity distribution affect the current-to-voltage relation on the boundary. Also, we should take inevitable measurement noise and modelling errors into account.

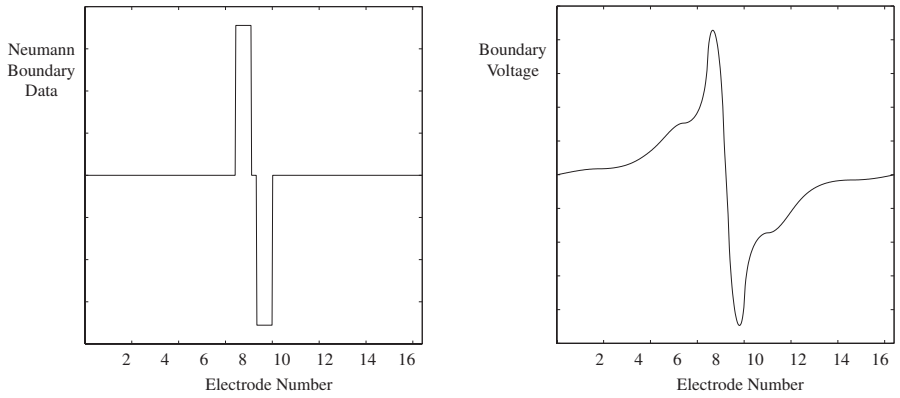

FIGURE 3. (a) Neumann boundary data of of the model in figure 2. We assumed that the current density underneath each current injection electrode is uniform. (b) Boundary voltage on 16 electrodes of the model. Here, we neglected the effects of electrode contact impedances.

3.2. **Inverse problem.** There has been a significant progress in theoretical study of the inverse problem in EIT. To provide a quick survey on these results, we denote the solution u of the Neumann boundary value problem in (5) by $u[\sigma, g]$ because it is determined uniquely by the conductivity distribution σ and the Neumann data g. To explain the inverse problem, we define the map $\Lambda_\sigma : g \rightarrow f$ by $\Lambda_\sigma[g] = u[\sigma, g]|_{\partial\Omega}$ where $u|_{\partial\Omega}$ is the restriction of u to $\partial\Omega$. The map Λ_σ is called the Neumann-to-Dirichlet (NtD) map. The reconstruction of σ requires us to invert the following map:

$$\sigma \rightarrow \{ \ (g_j \ , \ f_j) \ \}_{j=1}^N \qquad \text{with} \ \ f_j = \Lambda_\sigma[g_j]$$

for a given sequence of injection currents $\{g_j\}_{j=1}^N$.

The NtD map Λ_σ is closely related with the Neumann function restricted on $\partial\Omega$. The Neumann function $\mathcal{N}_\sigma(\mathbf{r}, \mathbf{r}')$ is the solution of the following Neumann problem: for each $\mathbf{r}$,

$$\begin{cases} \nabla_{\mathbf{r}'} \cdot (\sigma(\mathbf{r}')\nabla_{\mathbf{r}'}\mathcal{N}_\sigma(\mathbf{r}, \mathbf{r}')) = \delta(\mathbf{r} - \mathbf{r}') & \text{for all } \mathbf{r}' \in \Omega \\ \sigma(\mathbf{r}')\nabla_{\mathbf{r}'}\mathcal{N}_\sigma(\mathbf{r}, \mathbf{r}') \cdot \mathbf{n}(\mathbf{r}') = 0 & \text{for all } \mathbf{r}' \in \partial\Omega \end{cases}$$

where δ is the Dirac delta function. With the use of the Neumann function $\mathcal{N}_\sigma(\mathbf{r}, \mathbf{r}')$, we can represent $u[\sigma, g](\mathbf{r})$ in terms of the singular integral:

$$\begin{aligned} u[\sigma, g](\mathbf{r}) &= \textstyle\int_\Omega \delta(\mathbf{r} - \mathbf{r}') \ u[\sigma, g](\mathbf{r}') \ d\mathbf{r}' \\ &= \textstyle\int_\Omega \nabla \cdot (\sigma(\mathbf{r}')\nabla\mathcal{N}_\sigma(\mathbf{r}, \mathbf{r}')) \ u[\sigma, g](\mathbf{r}') \ d\mathbf{r}' \\ &= -\textstyle\int_\Omega \sigma(\mathbf{r}')\nabla\mathcal{N}_\sigma(\mathbf{r}, \mathbf{r}') \cdot \nabla u[\sigma, g](\mathbf{r}') \ d\mathbf{r}' \\ &= \textstyle\int_{\partial\Omega} \mathcal{N}_\sigma(\mathbf{r}, \mathbf{r}') \ g(\mathbf{r}') \ ds_{\mathbf{r}'}. \end{aligned}$$

Since $\Lambda_\sigma[g]$ is the restriction of $u[\sigma, g]$ to the boundary $\partial\Omega$, it can be represented as

$$\Lambda_\sigma[g](\mathbf{r}) = \int_{\partial\Omega} \mathcal{N}_\sigma(\mathbf{r}, \mathbf{r}')\, g(\mathbf{r}')\, ds_{\mathbf{r}'}, \quad \mathbf{r} \in \partial\Omega. \tag{7}$$

Therefore, the kernel $\mathcal{N}_\sigma(\mathbf{r}, \mathbf{r}')$ with $\mathbf{r}, \mathbf{r}' \in \partial\Omega$ can be viewed as a kind of an expression of the NtD map Λ_σ. Note that the map Λ_σ is sensitive to a change of the geometry of the surface $\partial\Omega$ since $\mathcal{N}_\sigma(\mathbf{r}, \mathbf{r}')$ is singular at $\mathbf{r} = \mathbf{r}'$.

It has been proved that the knowledge of Λ_σ is sufficient to uniquely determine σ provided that σ satisfies some minor regularity condition. For the uniqueness results, please see the previous works (Kohn and Vogelius 1984; Sylvester and Uhlmann 1986; Sylvester and Uhlmann 1987; Nachman 1988; Isakov 1988; Nachman 1996; Uhlmann 1999).

To reconstruct σ, it would be ideal if we could measure the full NtD map Λ_σ. However, in practice, it is not possible to get the complete knowledge of Λ_σ due to a limited number of electrodes and the difficulty in capturing the geometry of $\partial\Omega$.

It is well known that the inverse problem is highly nonlinear and insensitive to perturbations of an internal σ. The value of the voltage at a point inside the subject can be expressed as a weighted average of its neighboring voltages where the weights are determined by the conductivity distribution. To be precise, the conductivity equation $\nabla \cdot (\sigma(\mathbf{r})\nabla u(\mathbf{r})) = 0$ in a two dimensional domain can be written as the following discretized form of

$$u(x, y) \;\approx\; \frac{1}{\alpha} \sum_{i,j=\pm 1} \frac{\sigma(x, y)\, \sigma(x + i\Delta x, y + j\Delta y)}{\sigma(x, y) + \sigma(x + i\Delta x, y + j\Delta y)}\, u(x + i\Delta x, y + j\Delta y)$$

where $\alpha = \sum_{i,j=\pm 1} \frac{\sigma(x,y)\, \sigma(x+i\Delta x, y+j\Delta y)}{\sigma(x,y)+\sigma(x+i\Delta x, y+j\Delta y)}$. Therefore, the measured Dirichlet data is entangled in the global structure of the conductivity distribution in a highly nonlinear way and any internal conductivity value influences little to boundary measurements if $\sigma(x, y)$ is away from measuring points.

This ill-posed nature and severe nonlinearity make it very difficult for EIT to provide conductivity images with high quality. Increasing the matrix size of the corresponding numerical algorithm of the inverse problem for better spatial resolution makes the problem more ill-conditioned. Hence, having a larger number of electrodes beyond a certain limit may not help in producing better images since the deteriorated ill-conditioning problem may take over the benefit of additional information from the increased number of electrodes. For these reasons, the static EIT imaging is still far from clinical applications though the dynamic imaging has been tried in numerous clinical application areas (Holder 1993; Boone *1997; Metherall 1998).*

4. Basic idea of MREIT

For the static or absolute conductivity imaging, Magnetic Resonance Electrical Impedance Tomography (MREIT) has been lately proposed to overcome the technical limitations of EIT (Zhang 1992; Woo *1994; Ider 1998; Kwon 2002a; Oh 2003; Oh 2004).* Injected current in an electrically conducting subject produces

a magnetic field as well as an electric field. Noting that the magnetic field inside the subject can be measured by a non-contact method using an MRI scanner, we may transform the ill-posed problem in EIT into a well-posed one utilizing this additional information. MREIT is based on this new idea.

Since late 1980s, measurements of the internal magnetic flux density due to an injection current have been studied in Magnetic Resonance Current Density Imaging (MRCDI) to visualize the internal current density distribution (Joy *1989; Scott 1991; Scott 1992).* This requires an MRI scanner as a tool to capture internal magnetic flux density images. Once we obtain the magnetic flux density $\mathbf{B} = (B_x, B_y, B_z)$ due to an injection current I, we can produce an image of the corresponding internal current density distribution $\mathbf{J}$ from the Ampere's law $\mathbf{J} = \nabla \times \mathbf{B}/\mu_0$ where μ_0 is the magnetic permeability of the free space.

The basic concept of MREIT was proposed by combining EIT and MRCDI techniques (Zhang 1992; Woo *1994; Ider 1998; Kwon 2002a; Oh 2003; Oh 2004).* In MREIT, we measure the induced magnetic flux density $\mathbf{B}$ inside a subject due to an injection current I using an MRI scanner. Then, we may compute the internal current density $\mathbf{J}$ as is done in MRCDI. From $\mathbf{B}$ and/or $\mathbf{J}$, we can perceive the internal current pathways due to the conductivity distribution to be imaged.

However, if we try to utilize $\mathbf{J} = \nabla \times \mathbf{B}/\mu_0$ by measuring all three components of $\mathbf{B}$, there occurs a serious technical problem. Since any currently available MRI scanner measures only one component of $\mathbf{B}$ that is parallel to the direction of the main magnetic field of the MRI scanner, measuring all three orthogonal components of $\mathbf{B} = (B_x, B_y, B_z)$ requires subject rotations. These subject rotations are impractical and also cause other problems such as misalignments of pixels and movements of internal organs. Therefore, it is highly desirable to reconstruct conductivity images from only B_z instead of $\mathbf{B}$ where z is the direction of the main magnetic field of the MRI scanner. For this reason, most recent MREIT techniques focus on analyzing the information embedded in the measured B_z data to extract any constructive relations between B_z and the conductivity distribution to be imaged.

5. Mathematical formulation of MREIT

5.1. **Forward problem: magnetic flux density due to an injection current for a given conductivity.** As shown in figure 4, we assume an electrically conducting domain Ω with its boundary $\partial\Omega$ and an anisotropic conductivity distribution

$$\underline{\underline{\sigma}} = \begin{pmatrix} \sigma_{11} & \sigma_{12} & \sigma_{13} \\ \sigma_{12} & \sigma_{22} & \sigma_{23} \\ \sigma_{13} & \sigma_{23} & \sigma_{33} \end{pmatrix}$$

where $\underline{\underline{\sigma}}$ is a positive-definite symmetric matrix. We choose a pair of electrodes attached on $\partial\Omega$, for example, $\mathcal{E}_i$ and $\mathcal{E}_j$ to inject current I. Lead wires carrying the injection current I are denoted as $\mathcal{L}_i$ and $\mathcal{L}_j$. Then, the voltage u in Ω satisfies the following Neumann boundary value problem:

$$\begin{cases} \nabla \cdot \left[\underline{\underline{\sigma}}(\mathbf{r})\nabla u(\mathbf{r})\right] = 0 \text{ in } \Omega \\ -\underline{\underline{\sigma}}\nabla u \cdot \mathbf{n} = g \text{ on } \partial\Omega \end{cases} \tag{8}$$

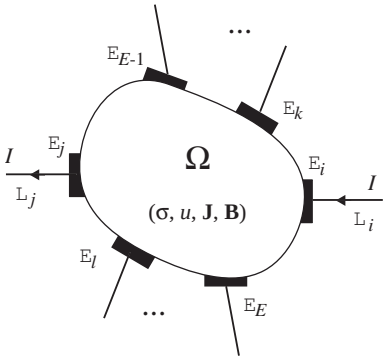

FIGURE 4. Electrically conducting subject Ω with a conductivity σ and voltage u distribution. Surface electrodes $\mathcal{E}_j, j = 1, \cdots, E$ are attached on the boundary $\partial\Omega$. Here, we assume that current is injected between the diagonal pair of electrodes $\mathcal{E}_i$ and $\mathcal{E}_j$.

where g is the Neumann boundary data due to the injection current. Knowing the voltage distribution u, the current density $\mathbf{J}$ is given by

$$\mathbf{J}(\mathbf{r}) = -\underline{\underline{\sigma}}(\mathbf{r})\nabla u(\mathbf{r}) \quad \text{in } \Omega. \tag{9}$$

We now consider the magnetic field produced by the injection current. The induced magnetic flux density $\mathbf{B}$ in Ω can be decomposed into three parts as

$$\mathbf{B}(\mathbf{r}) = \mathbf{B}_\Omega(\mathbf{r}) + \mathbf{B}_\mathcal{E}(\mathbf{r}) + \mathbf{B}_\mathcal{L}(\mathbf{r}) \quad \text{in } \Omega \tag{10}$$

where $\mathbf{B}_\Omega$, $\mathbf{B}_\mathcal{E}$ and $\mathbf{B}_\mathcal{L}$ are magnetic flux densities due to $\mathbf{J}$ in Ω, $\mathbf{J}$ in $\mathcal{E} = \mathcal{E}_i \cup \mathcal{E}_j$ and I in $\mathcal{L} = \mathcal{L}_i \cup \mathcal{L}_j$, respectively. From the Biot-Savart law,

$$\mathbf{B}_\Omega(\mathbf{r}) = \frac{\mu_0}{4\pi}\int_\Omega \mathbf{J}(\mathbf{r}') \times \frac{\mathbf{r}-\mathbf{r}'}{|\mathbf{r}-\mathbf{r}'|^3} dv', \tag{11}$$

$$\mathbf{B}_\mathcal{E}(\mathbf{r}) = \frac{\mu_0}{4\pi}\int_\mathcal{E} \mathbf{J}(\mathbf{r}') \times \frac{\mathbf{r}-\mathbf{r}'}{|\mathbf{r}-\mathbf{r}'|^3} dv' \tag{12}$$

and

$$\mathbf{B}_\mathcal{L}(\mathbf{r}) = \frac{\mu_0 I}{4\pi}\int_\mathcal{L} \mathbf{a}(\mathbf{r}') \times \frac{\mathbf{r}-\mathbf{r}'}{|\mathbf{r}-\mathbf{r}'|^3} dl' \tag{13}$$

where $\mathbf{a}(\mathbf{r}')$ is the unit vector in the direction of the current flow at $\mathbf{r}' \in \mathcal{L}$. From the Ampere's law, the current density $\mathbf{J}$ is also given by

$$\mathbf{J}(\mathbf{r}) = \frac{1}{\mu_0}\nabla \times \mathbf{B}(\mathbf{r}) \quad \text{in } \Omega. \tag{14}$$

We must have

$$\frac{1}{\mu_0}\nabla \times \mathbf{B}(\mathbf{r}) = -\underline{\underline{\sigma}}(\mathbf{r})\nabla u(\mathbf{r}) \text{ and } \nabla \cdot \mathbf{J}(\mathbf{r}) = 0 \quad \text{in } \Omega. \tag{15}$$

Numerical techniques in solving (8)-(14) are described by Lee *(2003b) with several examples.*

5.2. **Inverse problem: conductivity from Neumann-to-B_z (NtB_z) map.** Now, the problem of interest is to reconstruct an image of $\underline{\underline{\sigma}}$ in Ω from measured magnetic flux density and boundary voltage. For the uniqueness of a reconstructed isotropic conductivity image, it has been shown that we need to inject at least two currents using more than three electrodes and measure the corresponding magnetic flux densities (Kim *2003; Ider 2003)*.In addition, at least one one boundary voltage measurement is needed to recover the absolute values of the isotropic conductivity distribution. Since the measurement of $\mathbf{B} = (B_x, B_y, B_z)$ requires the impractical subject rotations, in this section, we assume that we measure only B_z without rotating the subject.

The description of the inverse problem in MREIT is based on the following setup. We place a subject Ω inside an MRI scanner and attach surface electrodes. When the number of electrodes is E, we can sequentially select one of $N \leq E \times (E-1)/2$ different pairs of electrodes to inject currents into the subject. Let the injection current between the j-th pair of electrodes be I_j for $j = 1, \cdots, N$ with $N \geq 2$. The current I_j produces a current density $\mathbf{J}_j = (J_x^j, J_y^j, J_z^j)$ inside the subject. The presence of the internal current density $\mathbf{J}_j$ and the current I_j in external lead wires generates a magnetic flux density $\mathbf{B}_j = (B_x^j, B_y^j, B_z^j)$ and $\mathbf{J}_j = \nabla \times \mathbf{B}_j/\mu_0$ holds inside the electrically conducting subject. We now assume that we have measured B_z^j for $j = 1, \cdots, N$.

Let u_j be the voltage due to the injection current I_j for $j = 1, \cdots, N$. Since $\underline{\underline{\sigma}}$ is approximately independent of injection currents, each u_j is a solution of the following Neumann boundary value problem:

$$\begin{cases} \nabla \cdot \big(\underline{\underline{\sigma}}(\mathbf{r})\nabla u_j(\mathbf{r})\big) = 0 & \text{in} \quad \Omega \\ -\underline{\underline{\sigma}}\nabla u_j \cdot \ \mathbf{n} = g_j & \text{on} \quad \partial\Omega \end{cases} \tag{16}$$

where g_j is the normal component of current density on the boundary of the subject for the injection current I_j. If $\underline{\underline{\sigma}}$, I_j, and electrode configuration are given, we can solve (16) for u_j using a numerical method such as FEM (Polydorides *2002; Lee 2003b)*. Now, we introduce a map relating B_z^j with the Neumann data g^j:

$$\Lambda_{\underline{\underline{\sigma}}}[g^j](\mathbf{r}) = B_z^j(\mathbf{r}), \quad \mathbf{r} \in \Omega.$$

We will call this map $\Lambda_{\underline{\underline{\sigma}}}$ by the Neumann-to-B_z map (NtB_z-map). According to the Biot- Savart law with a given g^j, $\Lambda_{\underline{\underline{\sigma}}}[g^j]$ is expressed as

$$\Lambda_{\underline{\underline{\sigma}}}[g^j](\mathbf{r}) = \frac{\mu_0}{4\pi}\int_\Omega \frac{\underline{\underline{\sigma}}(\mathbf{r}')\ [(x-x')\frac{\partial u^j}{\partial y}(\mathbf{r}') - (y-y')\frac{\partial u^j}{\partial x}(\mathbf{r}')]}{|\mathbf{r}-\mathbf{r}'|^3}\, d\mathbf{r}' \tag{17}$$

where u^j is the solution of (16). The inverse problem in MREIT is to reconstruct $\underline{\underline{\sigma}}$ from several NtB_z data, $\Lambda_{\underline{\underline{\sigma}}}[g^j], j = 1, \cdots, N$. In order for MREIT to be more practical, N should not be a large number.

6. MREIT image reconstruction techniques

When $\mathbf{B} = (B_x, B_y, B_z)$ is available, we may use $\mathbf{J}$ from (14) to reconstruct conductivity images using image reconstruction algorithms such as the J-substitution algorithm (Kwon *2002a; Khang 2002; Lee 2003a)*, current constrained voltage

scaled reconstruction (CCVSR) algorithm (Birgul *2003) and equipotential line methods (Ider 2003; Kwon 2002b; Lee 2004).* However, since these methods require the impractical subject rotation procedure, we describe algorithms utilizing only B_z data.

6.1. **Harmonic B_z algorithm.** Assuming the conductivity distribution of the subject isotropic, the harmonic B_z algorithm was developed as the first method to produce three-dimensional conductivity images from multi-slice measurements of B_z subject to at least two injection currents (Seo *2003; Oh 2003).* Based on the relation of $\nabla^2\mathbf{B} = -\mu_0 \nabla u \times \nabla\sigma$ observed by Scott *(Scott 1991), Seo (2003a)* derived the following expression that holds for each position in Ω.

$$\frac{1}{\mu_0}\nabla^2 B_z^j = \left(\frac{\partial\sigma}{\partial x}, \frac{\partial\sigma}{\partial y}\right)\cdot\left(\frac{\partial u_j}{\partial y}, -\frac{\partial u_j}{\partial x}\right) = \frac{\partial\sigma}{\partial x}\frac{\partial u_j}{\partial y} - \frac{\partial\sigma}{\partial y}\frac{\partial u_j}{\partial x}, \quad j = 1, \cdots, N. \tag{18}$$

Note that the magnetic flux density due to the injection current I_j along external lead wires becomes irrelevant by using $\nabla^2 B_z^j$. Using a matrix form, (18) becomes

$$\mathbf{U}\mathbf{s} = \mathbf{b} \tag{19}$$

where $\mathbf{U} = \begin{bmatrix} \frac{\partial u_1}{\partial y} & -\frac{\partial u_1}{\partial x} \\ \vdots & \vdots \\ \frac{\partial u_N}{\partial y} & -\frac{\partial u_N}{\partial x} \end{bmatrix}$, $\mathbf{s} = \begin{bmatrix} \frac{\partial\sigma}{\partial x} \\ \frac{\partial\sigma}{\partial y} \end{bmatrix}$, and $\mathbf{b} = \frac{1}{\mu_0}\begin{bmatrix} \nabla^2 B_z^1 \\ \vdots \\ \nabla^2 B_z^N \end{bmatrix}$.

For the case where two injection currents are used ($N = 2$), we can obtain $\mathbf{s}$ provided that two voltages u_1 and u_2 corresponding to two injection currents I_1 and I_2 satisfy

$$-\frac{\partial u_1}{\partial y}\frac{\partial u_2}{\partial x} + \frac{\partial u_1}{\partial x}\frac{\partial u_2}{\partial y} \neq 0. \tag{20}$$

We can argue that (20) holds for almost all positions within the subject since two current densities $\mathbf{J}_1$ and $\mathbf{J}_2$ due to appropriately chosen I_1 and I_2 will not have the same direction (Kim *2003; Ider 2003; Kim 2002).* We use N injection currents to better handle measurement noise in B_z and improve the condition number of $\mathbf{U}^T\mathbf{U}$ where $\mathbf{U}^T$ is the transpose of $\mathbf{U}$. Using the weighted regularized least square method suggested by Oh *(2003),*we can get $\mathbf{s}$ as

$$\mathbf{s} = \left(\tilde{\mathbf{U}}^T\tilde{\mathbf{U}} + \lambda\mathbf{I}\right)^{-1}\tilde{\mathbf{U}}^T\tilde{\mathbf{b}} \tag{21}$$

where λ is a positive regularization parameter, $\mathbf{I}$ is the 2×2 identity matrix, $\tilde{\mathbf{U}} = \mathbf{W}\mathbf{U}$, $\tilde{\mathbf{b}} = \mathbf{W}\mathbf{b}$ and $\mathbf{W} = \mathrm{diag}(w_1, \cdots, w_N)$ is an $N \times N$ diagonal weight matrix. Oh *(2003)* discussed different ways of determining the value of λ and the weight w_j. Computing (21) for each position or pixel, we obtain a distribution of $\mathbf{s} = \begin{bmatrix} \frac{\partial\sigma}{\partial x} & \frac{\partial\sigma}{\partial y} \end{bmatrix}^T$ inside the subject.

We now tentatively assume that the imaging slice $\mathcal{S}$ is lying in the plane $\{z = 0\}$ and the conductivity value at a fixed position $\mathbf{r}_0 = (x_0, y_0, 0)$ on its boundary $\partial\mathcal{S}$ is 1. For a moment, we denote $\mathbf{r} = (x, y)$, $\mathbf{r}' = (x', y')$ and $\sigma(x, y, 0) = \sigma(\mathbf{r})$. In order to compute σ from $\nabla\sigma = (\frac{\partial\sigma}{\partial x}, \frac{\partial\sigma}{\partial y})$, Oh *(2003)* suggested a layer potential

technique that turns out to denoising advantage. The σ on the fixed plane $z = 0$ can be expressed as

$$\sigma(\mathbf{r}) = -\int_{\mathcal{S}} \nabla_{\mathbf{r}'}\Psi\left(\mathbf{r}-\mathbf{r}'\right)\cdot\nabla\sigma(\mathbf{r}')d\mathbf{r}' + \int_{\partial\mathcal{S}} \mathbf{n}_{\mathbf{r}'}\cdot\nabla_{\mathbf{r}'}\Psi(\mathbf{r}-\mathbf{r}')\,\tilde{\sigma}(\mathbf{r}')dl_{\mathbf{r}'} \tag{22}$$

where $\Psi(\mathbf{r}-\mathbf{r}') = \frac{1}{2\pi}\log|\mathbf{r}-\mathbf{r}'|$ and $\tilde{\sigma}$ denotes the conductivity restricted at the boundary $\partial\mathcal{S}$. Moreover, $\tilde{\sigma}$ satisfies

$$\frac{\tilde{\sigma}(\mathbf{r})}{2} + \frac{1}{2\pi}\int_{\partial\mathcal{S}} \frac{(\mathbf{r}-\mathbf{r}')\cdot\mathbf{n}_{\mathbf{r}'}}{|\mathbf{r}-\mathbf{r}'|^2}\,\tilde{\sigma}(\mathbf{r}')dl'_{\mathbf{r}} = \frac{1}{2\pi}\int_{\mathcal{S}} \frac{(\mathbf{r}-\mathbf{r}')\cdot\nabla\sigma(\mathbf{r}')}{|\mathbf{r}-\mathbf{r}'|^2}d\mathbf{r}' \tag{23}$$

It is well known that the solvability of the integral equation (23) for $\tilde{\sigma}$ is guaranteed for a given right side of (23). For this solvability, see the book (Folland 1976). Since $\nabla\sigma$ is known in $\mathcal{S}$, so does the right side of (23). This enables us to obtain the value $\tilde{\sigma}$ by solving the integral equation (23). Now, we can compute the conductivity σ in $\mathcal{S}$ by substituting the boundary conductivity $\tilde{\sigma}$ into (22).

The process of solving (21) for each pixel and (23) for each imaging slice can be repeated for all imaging slices of interest within the subject as long as the measured data B_z are available for the slices. Furthermore, we can apply the method described in this section to any imaging slice of axial, coronal and sagittal direction.

As expressed in (16), voltages u_j depend on the unknown true isotropic conductivity σ and, therefore, we do not know the matrix $\mathbf{U}$ corresponding to σ. This requires us to use the iterative algorithm described below. For $j = 1, \cdots, N$, we sequentially inject current I_j through a chosen pair of electrodes and measure the z-component of the induced magnetic flux density B_z^j. For each injection current I_j, we also measure boundary voltages $u_j\,|_{\partial\mathcal{S}}$ on electrodes not injecting the current I_j. Then, the $\nabla^2 B_z$ algorithm is as follows.

1. Let $n = 0$ and assume an initial conductivity distribution σ_0.
2. Compute u_j^n by solving the following Neumann boundary value problems for $j = 1, \cdots, N$:

$$\begin{cases} \nabla\cdot\left(\sigma_n\nabla u_j^n\right) = 0 & \text{in } \Omega \\ -\sigma_n\nabla u_j^n\cdot\ \mathbf{n} = g_j & \text{on } \partial\Omega. \end{cases} \tag{24}$$

3. Compute σ_{n+1} using (21), (22) and (23). Scale σ_{n+1} using the measured boundary voltages $u_j\,|_{\partial\mathcal{S}}$ and the corresponding computed ones $u_j^n\,|_{\partial\mathcal{S}}$.
4. If $\|\sigma_{n+1}-\sigma_n\|_2 < \epsilon$, go to Step 5. Here, ϵ is a given tolerance. Otherwise, set $n \leftarrow (n+1)$ and go to Step 2.
5. If needed, compute current density images as $\mathbf{J}_j \leftarrow -\sigma_{n+1}\nabla u_j^M$ where u_j^M is a solution of the boundary value problem in (16) with σ_{n+1} replacing σ.

6.2. **Gradient B_z decomposition algorithm.** After the introduction of the harmonic B_z algorithm, there has been an effort to improve its performance especially in terms of the way we numerically differentiate the measured noisy B_z data. Based on a novel analysis utilizing the Helmhortz decomposition, Park *(2004b)*suggested the gradient B_z decomposition algorithm. Here, we also assume that the conductivity is isotropic.

In order to explain the algorithm, let us assume $\Omega = D \times [-\delta, \delta] = \{\mathbf{r} = (x, y, z) | (x, y) \in D,\ -\delta < z < \delta\}$ is an electrically conducting subject where D is a two dimensional smooth simply connected domain. Let u be the solution of the Neumann boundary value problem (8) or (16) with the Neumann data g. We parameterize ∂D as $\partial D := \{(x(t), y(t)) : 0 \le t \le 1\}$ and define $\tilde{g}(x(t), y(t), z) := \int_0^t g((x(t), y(t), z))\sqrt{|x'(t)|^2 + |y'(t)|^2}dt$ for $(x, y, z) \in \partial D \times (-\delta, \delta)$.

The gradient B_z decomposition algorithm is based on the following key identity:

$$\sigma = \frac{\left| -\left(\frac{\partial H}{\partial y} + \Lambda_x[u]\right)\frac{\partial u}{\partial x} + \left(\frac{\partial H}{\partial x} + \Lambda_y[u]\right)\frac{\partial u}{\partial y}\right|}{(\frac{\partial u}{\partial x})^2 + (\frac{\partial u}{\partial y})^2} \quad \text{in } \Omega \tag{25}$$

where

$$\Lambda_x[u] := \frac{\partial \psi}{\partial y} - \frac{\partial W_z}{\partial x} + \frac{\partial W_x}{\partial z} \quad \text{and} \quad \Lambda_y[u] := \frac{\partial \psi}{\partial x} + \frac{\partial W_z}{\partial y} - \frac{\partial W_y}{\partial z} \quad \text{in } \Omega$$

and

$$H = \phi + \frac{1}{\mu_0} B_z, \qquad W(\mathbf{r}) := \int_{\Omega_\delta} \frac{1}{4\pi|\mathbf{r} - \mathbf{r}'|} \frac{\partial(\sigma \nabla u(\mathbf{r}'))}{\partial z} d\mathbf{r}'.$$

Here, ϕ and ψ are solutions of the following equations:

$$\begin{cases} \nabla^2 \phi = 0 \quad \text{in } \Omega \\ \phi = \tilde{g} - \frac{1}{\mu_0} B_z \quad \text{on } \partial\Omega_{side} \\ \frac{\partial \phi}{\partial z} = -\frac{1}{\mu_0}\frac{\partial B_z}{\partial z} \quad \text{on } \partial\Omega_{tb} \end{cases} \quad \text{and} \quad \begin{cases} \nabla^2 \psi = 0 \quad \text{in } \Omega \\ \nabla\psi \cdot \tau = \nabla \times W \cdot \tau \quad \text{on } \partial\Omega_{side} \\ \frac{\partial \psi}{\partial z} = -\nabla \times W \cdot \epsilon_z \quad \text{on } \partial\Omega_{tb} \end{cases}$$

where $\epsilon_z = (0, 0, 1)$, $\partial\Omega_{side} = \partial D \times (-\delta, \delta)$, Ω_{tb} is the top and bottom surfaces of Ω, and $\tau := (-n_y, n_x, 0)$ is the tangent vector on the lateral boundary $\partial D \times (-\delta, \delta)$.

Since the term u in (25) is a highly nonlinear function of σ, the identity (25) can be viewed as an implicit reconstruction formula for σ. It should be noticed that we can not identify σ with a single g using (25). Hence, we may use an iterative reconstruction scheme with multiple Neumann data $g_j, j = 1, \cdots, N$ to find σ. Let u_j^m be the solution of (16) with $\sigma = \sigma_m$ and g_j. Then, the reconstructed σ is the limit of a sequence σ^m that is obtained by the following formula:

$$\sigma_{m+1} = \frac{\sum_{i=1}^N \left| -\left(\frac{\partial H_i}{\partial y} + \Lambda_x[u_i^m]\right)\frac{\partial u_i^m}{\partial x} + \left(\frac{\partial H_i}{\partial x} + \Lambda_y[u_i^m]\right)\frac{\partial u_i^m}{\partial y}\right|}{\sum_{i=1}^N \left[\left(\frac{\partial u_i^m}{\partial x}\right)^2 + \left(\frac{\partial u_i^m}{\partial y}\right)^2\right]}.$$

6.3. **Anisotropic conductivity image reconstruction algorithm.** Up to now, all MREIT techniques have assumed an isotropic conductivity distribution to simplify the underlying mathematical theory of the image reconstruction problem. However, most biological tissues are known to have anisotropic conductivity values. The ratio of the anisotropy depends on the type of tissue and the human skeletal muscle, for example, shows the anisotropy of up to one to ten between the longitudinal and transversal direction. Hence, clinical applications of MREIT require us to develop an anisotropic conductivity image reconstruction algorithm.

Lately, a new algorithm that can handle anisotropic conductivity distributions has also been suggested by Seo *(2004b)*. This algorithm requires at least 7 different

currents, while the previous MREIT reconstruction algorithms for isotropic one require at least 2 different currents.

The reconstruction algorithm begins with the identity $\frac{1}{\mu_0}\nabla^2 B_z = \partial_y J_x - \partial_x J_y$ that can be written as

(26)
$$\begin{aligned}\tfrac{1}{\mu_0}\nabla^2 B_z = {} & (-\partial_y\sigma_{11} + \partial_x\sigma_{12})u_x + (-\partial_y\sigma_{12} + \partial_x\sigma_{22})u_y + (-\partial_y\sigma_{13} + \partial_x\sigma_{23})u_z \\ & +\sigma_{12}(u_{xx} - u_{yy}) + (-\sigma_{11} + \sigma_{22})u_{xy} + \sigma_{23}u_{xz} - \sigma_{13}u_{yz}.\end{aligned}$$

where u is the solution of (8). The above identity (26) is true for each u_j with $j = 1, \cdots, N$. In this subsection, u_j will be denoted by u^j as a matter of convenience. We have

$$\mathbf{U}\mathbf{s} = \mathbf{b} \tag{27}$$

where

$$\mathbf{b} = \frac{1}{\mu_0}\begin{bmatrix} \nabla^2 B_z^1 \\ \vdots \\ \nabla^2 B_z^N \end{bmatrix}, \qquad \mathbf{s} = \begin{bmatrix} -\partial_y\sigma_{11} + \partial_x\sigma_{12} \\ -\partial_y\sigma_{12} + \partial_x\sigma_{22} \\ -\partial_y\sigma_{13} + \partial_x\sigma_{23} \\ \sigma_{12} \\ -\sigma_{11} + \sigma_{22} \\ \sigma_{23} \\ \sigma_{13} \end{bmatrix}$$

and

$$\mathbf{U} = \begin{bmatrix} u_x^1 & u_y^1 & u_z^1 & u_{xx}^1 - u_{yy}^1 & u_{xy}^1 & u_{xz}^1 & -u_{yz}^1 \\ \vdots & \vdots & \vdots & \vdots & \vdots & \vdots & \vdots \\ u_x^N & u_y^N & u_z^N & u_{xx}^N - u_{yy}^N & u_{xy}^N & u_{xz}^N & -u_{yz}^N \end{bmatrix}.$$

We do not know the true $\underline{\underline{\sigma}}$ and therefore the matrix $\mathbf{U}$ is unknown. This requires us to use an iterative procedure to compute $\mathbf{s}$ in (27) as in the previous section. For now, let us assume that we have computed all seven terms of $\mathbf{s}$. From $\mathbf{s}$, we can immediately determine

$$\sigma_{12}(\mathbf{r}) = s_4(\mathbf{r}), \quad \sigma_{13}(\mathbf{r}) = s_7(\mathbf{r}) \quad \text{and} \quad \sigma_{23}(\mathbf{r}) = s_6(\mathbf{r}), \qquad \mathbf{r} \in \Omega. \tag{28}$$

To determine σ_{11} and σ_{22} from $\mathbf{s}$, we use the relation between $\mathbf{s}$ and $\underline{\underline{\sigma}}$;

$$\frac{\partial\sigma_{11}}{\partial x} = s_2 - \frac{\partial s_5}{\partial x} + \frac{\partial s_4}{\partial y} \quad \text{and} \quad \frac{\partial\sigma_{11}}{\partial y} = -s_1 + \frac{\partial s_4}{\partial x}. \tag{29}$$

Using the above relation, we can derive the following expression of σ_{11}:

$$\begin{aligned}\sigma_{11}(a,b,z) = {} & \int_{\Omega_z}\left[\left(-s_2 + \tfrac{\partial s_5}{\partial x} - \tfrac{\partial s_4}{\partial y}\right)\tfrac{\partial}{\partial x}\Psi(x-a, y-b)\right]dxdy \\ & + \int_{\Omega_z}\left[\left(s_1 - \tfrac{\partial s_4}{\partial x}\right)\tfrac{\partial}{\partial y}\Psi(x-a, y-b)\right]dxdy \\ & + \int_{\partial\Omega_z}\tilde{\sigma}_{11}(x,y,z)\left[\tilde{\mathbf{n}}\cdot\nabla_{x,y}\Psi(x-a, y-b)\right]dl_{x,y}\end{aligned} \tag{30}$$

where $\Omega_z = \{(x,y) : (x,y,z) \in \Omega\}$, $\Psi(x,y) = \frac{1}{2\pi}\log\sqrt{x^2+y^2}$, and $\tilde{\sigma}_{11}$ is σ_{11} restricted at the boundary $\partial\Omega_z$. In the representation formula (30), the reconstruction of σ_{11} inside Ω_z requires the computation of $\tilde{\sigma}_{11}$ along the boundary $\partial\Omega_z$.

Computation of $\tilde{\sigma}_{11}$ can be done by solving the following integral equation:

$$\begin{aligned} &\tfrac{1}{2}\tilde{\sigma}_{11}(a^*,b^*,z) - \textstyle\int_{\partial\Omega_z} \tilde{\sigma}_{11}(x,y,z)\,[\tilde{\mathbf{n}}\cdot\nabla_{x,y}\Psi(x-a^*,y-b^*)]\,dl_{x,y} \\ &\quad = \textstyle\int_{\Omega_z}\left[\left(-s_2+\frac{\partial s_5}{\partial x}-\frac{\partial s_4}{\partial y}\right)\frac{\partial}{\partial x}\Psi(x-a^*,y-b^*)\right]dxdy \\ &\qquad + \textstyle\int_{\Omega_z}\left[\left(s_1-\frac{\partial s_4}{\partial x}\right)\frac{\partial}{\partial y}\Psi(x-a^*,y-b^*)\right]dxdy. \end{aligned} \tag{31}$$

for $(a^*,b^*)\in\partial\Omega_z$. Substituting the computed $\tilde{\sigma}_{11}$ on $\partial\Omega_z$ into the boundary integral in the right side of (30) yields the explicit representation of the internal σ_{11}. Similarly, we can compute the component σ_{22}.

Now it remains to find the last component σ_{33} whose information is missing in (27). We use the physical law $\nabla\cdot\mathbf{J}=0$ that can be rewritten as

$$\partial_z\sigma_{33}\,u_z+\sigma_{33}\,u_{zz}=\partial_x J_x+\partial_y J_y-\partial_z(\sigma_{13}u_x+\sigma_{23}u_y) \tag{32}$$

Gathering the above identity (32) for u^j with $j=1,\cdots,N$ leads to

$$\begin{bmatrix} u_z^1 & u_{zz}^1 \\ \vdots & \vdots \\ u_z^N & u_{zz}^N \end{bmatrix}\begin{bmatrix} \sigma_{33} \\ \partial_z\sigma_{33}\end{bmatrix}=\begin{bmatrix}\psi^1\\ \vdots\\ \psi^N\end{bmatrix} \tag{33}$$

where

$$\psi^j=\partial_x J_x^j+\partial_y J_y^j-\partial_z(\sigma_{13}u_x^j+\sigma_{23}u_y^j),\quad j=1,\cdots,N.$$

Note that the term ψ^j in the right side of (33) is determined by $\sigma_{11},\sigma_{12},\sigma_{13},\sigma_{22},\sigma_{23}$ and u^n. Since we have determined $\sigma_{11},\sigma_{12},\sigma_{13},\sigma_{22}$ and σ_{23} from $\mathbf{s}$, we can compute σ_{33} by a natural iterative process using (33).

6.4. **Other algorithms.** There are other algorithms such as the variational gradient B_z algorithm (Park *2004a).* All of these algorithms are quite successful in numerical simulations and experimental studies using a relatively large amount of injection current. Therefore, the algorithm development in MREIT should be focused on how to handle random and systematic noise in the measured B_z data. It should include efficient denoising techniques utilizing the fundamental properties of the induced magnetic flux density. Since conventional MR images providing excellent structural information are always available in MREIT, we may incorporate this *a priori* information in MREIT conductivity image reconstructions.

7. Measurement techniques in MREIT

Let z be the coordinate that is parallel to the direction of the main magnetic field $\mathbf{B}_0$ of an MRI scanner. Using a constant current source and a pair of surface electrodes, we sequentially inject two current pulses of $I^{\pm}$ and $I^{\mp}$ synchronized with the standard spin echo pulse sequence shown in figure **??**. The application of the injection current during MR imaging induces a magnetic flux density $\mathbf{B}=(B_x,B_y,B_z)$. Since the magnetic flux density $\mathbf{B}$ produces inhomogeneity of the main magnetic field changing $\mathbf{B}_0$ to $(\mathbf{B}_0+\mathbf{B})$, it causes phase changes that are

proportional to the z-component of $\mathbf{B}$, that is B_z. Then, the corresponding MRI signals are

$$S^{I^{\pm}}(m,n) = \iint_{-\infty}^{\infty} M(x,y) e^{j\delta(x,y)} e^{j\gamma B_z(x,y)T_c} e^{j(xm\Delta k_x + yn\Delta k_y)} dxdy \tag{34}$$

and

$$S^{I^{\mp}}(m,n) = \iint_{-\infty}^{\infty} M(x,y) e^{j\delta(x,y)} e^{-j\gamma B_z(x,y)T_c} e^{j(xm\Delta k_x + yn\Delta k_y)} dxdy. \tag{35}$$

Here, M is the transverse magnetization, δ is any systematic phase error, $\gamma = 26.75 \times 10^7$ rad/Tesla is the gyromagnetic ratio of the hydrogen, T_c is the duration of current pulses.

Two-dimensional discrete Fourier transformations of $S^{I^{\pm}}(m,n)$ and $S^{I^{\mp}}(m,n)$ result in two complex images of $\mathcal{M}_c^{\pm}(x,y)$ and $\mathcal{M}_c^{\mp}(x,y)$, respectively. Dividing the two complex images, we get

$$\mathrm{Arg}\left(\frac{\mathcal{M}_c^{\pm}(x,y)}{\mathcal{M}_c^{\mp}(x,y)}\right) = \mathrm{Arg}\left(e^{j2\gamma B_z(x,y)T_c}\right) = \tilde{\Phi}_z(x,y)$$

where $\mathrm{Arg}(\omega)$ is the principal value of the argument of the complex number ω. Since $\tilde{\Phi}_z$ is wrapped in $-\pi < \tilde{\Phi}_z \leq \pi$, we must unwrap $\tilde{\Phi}_z$ to obtain Φ_z (Ghiglia *1998)* Finally, we get

$$B_z(x,y) = \frac{1}{2\gamma T_c}\Phi_z(x,y). \tag{36}$$

Scott *et al.* analyzed the Gaussian random noise in measured B_z (Scott *1992)* Denoting the standard deviation of the Gaussian random noise as s_B, it can be estimated as

$$s_B = \frac{1}{2\gamma T_c \Upsilon_M} \tag{37}$$

where Υ_M is the signal-to-noise ratio (SNR) of the corresponding MR magnitude image $M(x,y)$ in (34) or (35). The noise standard deviation is inversely proportional to the size of each pixel since Υ_M in (37) is proportional to the size. With T_c =50 ms, we obtain $s_B = 1.43 \times 10^{-9}$ and 5.68×10^{-9} Tesla when Υ_M=50 and 25, respectively.

In MREIT, we are interested in the SNR of measured magnetic flux density images and it is mainly determined by the noise standard deviation s_B in (37), amount of injection current, size of the subject, and electrode configuration. To reduce s_B, we must increase the SNR of the MR magnitude image, Υ_M in (37). This can be done by increasing the voxel size, number of averaging, strength of the main magnetic field, and so on. In doing so, it is inevitable to sacrifice the spatial and/or temporal resolution to some extent.

Regarding the amount of injection currents, it should be lower than the level that can stimulate muscle or nerve tissues. Although the amount depends on several factors such as the size and shape of electrodes, anatomical structure, and type of tissues, it is desirable to conform to the safety guideline. According to the guideline, the current should be limited below 0.1 mA at the frequency range of below 1 KHz.

The safety limit increases as frequency goes up and a current up to 5 mA is allowed at 50 KHz and beyond.

From the Biot-Savart law in (11), we can see that the magnitude of magnetic flux density at one point is strongly dependent on the current density near the point. The current density distribution inside the subject could be quite inhomogeneous and very low current density could appear at some local regions depending on the dimension of the subject and electrode configuration. If we use small electrodes compared with the subject size, the current density at the vicinity of the electrodes will be much higher than that in the far region. To alleviate the spatial dependency of the SNR, it may be desirable to use electrodes with an appropriate size.

8. Progress in MREIT images

Since MREIT is still at its early stage of development, most of the published MREIT conductivity images are from numerical simulations and phantom experiments (Oh *2003; Oh 2004; Seo 2003a; Park 2004b; Park 2004a; Seo 2004b).* In this section, we describe experimental results obtained by using an MREIT system based on a 3 Tesla MRI scanner.

In order to verify the spatial resolution and accuracy of the reconstructed conductivity image. Oh *(2004)* constructed a resolution phantom of which design is shown in figure 5(a). Inside the phantom, six cotton threads with diameters of 2, 3 and 4 mm are vertically placed. With the background solution of 0.63 S/m, threads had a different conductivity value than the solution. They also put two wedge-shaped sponges facing each other inside the phantom. Since the sponges had different densities, the conductivity of each sponge was also different from the solution. Figure 5(b) is an MR magnitude image of the phantom at the middle imaging slice. Figure 5(c), (d) and (e) are reconstructed conductivity images at three imaging slices with different vertical positions. We can observe that six threads are clearly distinguished suggesting the spatial resolution of about 2 mm with injection currents of a sufficient amount. Depending on the imaging slice, areas of two rectangular sponge regions change and this indicates that the three-dimensional conductivity distribution with vertical variations could be reconstructed.

Though there are still several technical problems to be solved including the reduction of the amount of injection current, MREIT has the potential to provide cross-sectional conductivity images with better accuracy and spatial resolution. Reconstructed static conductivity images will allow us to obtain internal current density images for any arbitrary injection currents and electrode configurations.

9. Conclusions and Outlook

EIT has been an active research area since early 1980s. Struggling to overcome the ill-posed nature of the inverse problem in EIT image reconstructions, numerous techniques have been suggested. Even with these efforts, further improvements in image quality are needed for successful clinical applications. Three-dimensional dynamic EIT imaging with a wireless miniaturized EIT system is believed to make the next breakthrough in EIT technology. Obtaining and utilizing the accurate

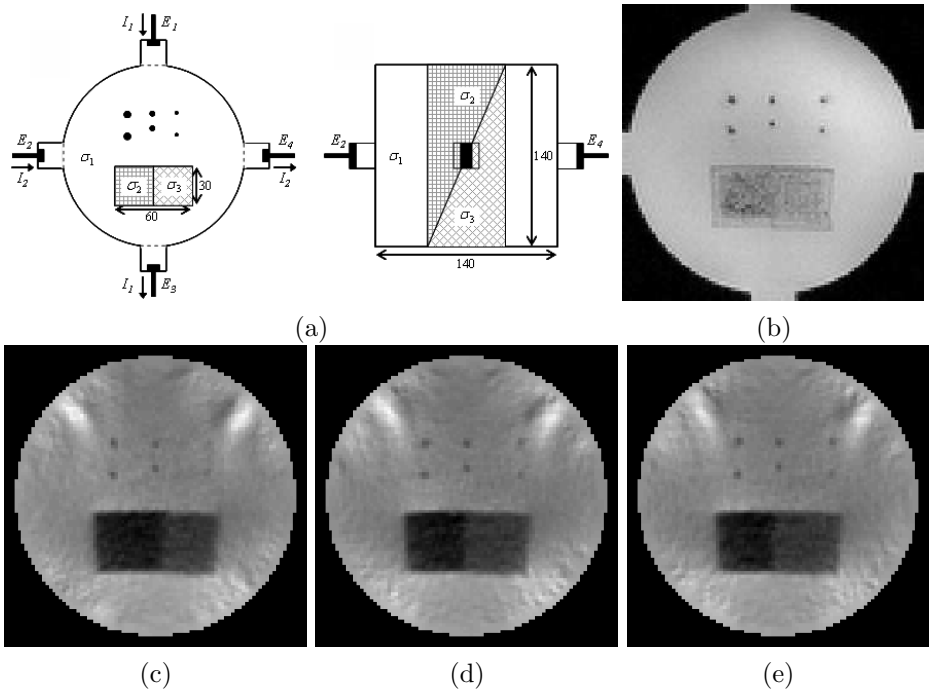

FIGURE 5. MREIT experiment using a resolution phantom. (a) Phantom design including six cotton threads with 2, 3 and 4 mm diameters and two wedge-shaped sponges facing each other. (b) MR magnitude image of the phantom at the middle imaging slice. (c), (d) and (e) are reconstructed conductivity images of the phantom at three different imaging slices with different vertical positions.

data for the shape and size of a subject with electrode positions, static EIT imaging could be improved. However, since the ill-posedness in EIT still remains anyway, we should not expect EIT to compete with other medical imaging modalities in terms of spatial resolution. The significance of EIT should be emphasized based on the fact that it provides the information on electrical properties of biological tissues. Since this kind of information is not available from any other imaging modality, EIT should keeping finding unique application areas especially in dynamic functional imaging. Based on the frequency dependent characteristics of tissue conductivity and permittivity, multi-frequency three-dimensional EIT imaging is also quite promising.

The latest research outcomes in MREIT show the definite feasibility of the technique for high-resolution static conductivity imaging. With many possible clinical and biological applications in mind, future research direction in MREIT should follow the way to reduce the amount of the injection current. Anisotropic conductivity imaging is believed to be pursuable in MREIT even though it is not feasible in EIT.

MREIT should always include the current density imaging to provide more information from the same measured data. The performance of the MRI system itself has been greatly enhanced to make 3 Tesla systems available to clinical settings. The progress in MREIT techniques will follow this trend.

The lesion estimation technique can be viewed as a parametric EIT imaging. Providing the core information on lesions inside a subject, it can effectively avoid the ill-posedness in EIT imaging. Considering the fact that there are numerous medical and also industrial applications, further developments in its theory, algorithms, and measurement techniques are desirable. Currently, the potential applicability of the technique to breast cancer detection is the strongest motivation for future research efforts.

Acknowledgments

This work was supported by grant R11-2002-103 from Korea Science and Engineering Foundation.

References

[1] Adey W, Kado R and Didio J 1962 Impedance measurements in brain tissue of animals using microvolt signals *Exp. Neruol.* **5** 47-66

[2] Aladjolova N A 1964 Slow electrical processes in the brain *Prog. in Brain Res.* **7** 155-237

[3] Alessandrini G, Isakov V and Powell J 1995 Local uniqueness in the inverse problem with one measurement *Trans. Amer. Math. Soc.* **347** 3031-41

[4] Barber D.C. and Brown B.H. 1984 Applied Potential Tomography (Review Article) *J. Phys. E:Sci. Instrum* **17** 723 - 733

[5] Beravs K, White D, Sersa I and Demsar F 1997 Electric current density imaging of bone by MRI *Magn. Reson. Imag.* **15** 909-15

[6] Beravs K, Frangez R, Gerkis A N and Demsar F 1999a Radiofrequency current density imaging of kainate-evoked depolarization *Magn. Reson. Imag.* **42** 136-40

[7] Beravs K, Demsar A and Demsar F 1999b Magnetic resonance current density imaging of chemical processes and reactions *J. Magn. Reson.* **137** 253-7

[8] Birgul O, Ozbekl O, Eyuboglul B M and Ider Y Z 2001 Magnetic resonance conductivity imaging using 0.15 tesla MRI scanner *Proc. 23rd. Ann. Int. Conf. IEEE Eng. Med. Biol. Soc.*

[9] Birgul O, Eyuboglu B M and Ider Y Z 2003 Current constrained voltage scaled reconstruction (CCVSR) algorithm for MR-EIT and its performance with different probing current patterns *Phys. Med. Biol.* **48** 653-71

[10] Bodurka J, Jesmanowicz A, Hyde J S, Xu H, Estkowski L and Li S J 1999 Current-induced magnetic resonance phase imaging *J. Magn. Reson.* **137** 265-71

[11] Bodurka J and Bandettini P A 2002 Toward direct mapping of neural activity: MRI detection of ultraweak, transient magnetic field changes *Magn. Reson. Med.* **47** 1052-8

[12] Boone K, Barber D and Brown B 1997 Imaging with electricity: report of the European concerted action on impedance tomography *J. Med. Eng. Tech.* **21** 201-32

[13] Brown B.H. and Seagar A.D. 1987 The Sheffield Data Collection System. *Clin. Phys. Physiol. Meas.* **8**(Suppl. A): 91 - 97.

[14] Burnett D S 1987 *Finite Element Analysis* (Reading, MA: Addison-Wesley)

[15] Carter M A 1995 *RF Current Density Imaging with a Clinical Magnetic Resonance Imager* (MS Thesis, University of Toronto, Canada)

[16] Chan T, Marquina A and Mulet P 2000 High-order total variation-based image restoration *SIAM J. Sci. Comput.* **22** 503-16

[17] Cheney M and Isaacson D 1992 Distinguishability in impedance imaging *IEEE Trans. Biomed. Eng.***39** 852-60

[18] Cheney M, Isaacson D, and Newell J C 1999 Electrical impedance tomography *SIAM Review* **41** pp. 85–101.

[19] Cole K S and Curtis H J 1939 Electrical impedance of the squid giant axon during activity *J. Gen. Physiol.* **22** 649-70

[20] Cole K S 1949 Dynamic electrical characteristics of squid axon membrane *Arch. Sci. Physiol.* **3** 253-8

[21] Eyuboglu M, Birgul O and Ider Y Z 2001 A dual modality system for high resolution-true conductivity imaging *Proc. XI Int. Conf. Elec. Bioimpedance (ICEBI)* 409-13

[22] Eyuboglu M, Reddy R and Leigh J S 1998 Imaging electrical current density using nuclear magnetic resonance *Elektrik* **6** 201-14

[23] Folland G 1976 *Introduction to Partial Differential Equations* (Princeton, NJ, USA: Princeton University Press)

[24] Friedman A and Isakov V 1989 On the uniqueness in the inverse conductivity problem with one measurement *Indiana Univ. Math. J.* **38** 553-80

[25] Gamba H R and Delpy D T 1998 Measurement of electrical current density distribution within the tissues of the head by magnetic resonance imaging *Med. Biol. Eng. Comp.* **36** 165-70

[26] Gamba H R, Bayford D and Holder D 1999 Measurement of electrical current density distribution in a simple head phantom with magnetic resonance imaging *Phys. Med. Biol.* **44** 281-91

[27] Geddes L A and Baker L E 1967 The specific resistance of biological material: a compendium of data for the biomedical engineer and physiologist *Med. Biol. Eng.* **5** 271-93

[28] Gerkis A N 1996 *An Enhanced RF Current Density Imaging Technique for Imaging Biological Media* MS Thesis, University of Toronto, Canada

[29] Ghiglia D C and Pritt M D 1998 *Two-Dimensional Phase Unwrapping: Theory, Algorithms and Software* (New York: Wiley Interscience)

[30] Greenleaf A, Lassas M and Uhlmann G 2003 Anisotropic conductivities that cannot be detected by EIT *Physiol. Meas.* **24** 413-9

[31] Grimnes G and Martinsen O G 2000 *Bioimpedance and Bioelectricity Basics* (London, UK: Academic Press)

[32] Haemmerich D, Staelin S T, Tsai J Z, Tungjitkusolmun S, Mahvi D M and Webster J G 2003 *In vivo* electrical conductivity of hepatic tumours *Physiol. Meas.* **24** 251-60

[33] Holder D.S.1993 Physiological Constraints to Imaging Brain Function Using Scalp Electrodes. *Clinical and Physiological Applications of Electrical Impedance Tomography. D. Holder (ed). UCL Press, London* Chapter **21** 185 - 200

[34] Ider Y Z and Birgul O 1998 Use of the magnetic field generated by the internal distribution of injected currents for Electrical Impedance Tomography (MR-EIT) *Elektrik* **6** 215-25

[35] Ider Y Z, Onart S and Lionheart W R B 2003 Uniqueness and reconstruction in magnetic resonance.electrical impedance tomography (MR.EIT) *Physiol. Meas.* **24** 591-604

[36] Isakov V 1988 On uniqueness of recovery of a discontinuous conductivity coefficient *Comm. Pure Appl. Math.* **41** 856-77

[37] Isaacson D. 1986 Distinguishability of Conductivities by Electric Current Computed Tomography *IEEE Trans. Med. Imag.* **41** 91 - 95.

[38] Jossinet J and Schmitt M 1999 A review of parameters for the bioelectrical characterization of breast tissue *Ann. New York Academy of Sci.* **873** 30-41

[39] Joy M L G, Scott G C and Henkelman R M 1989 In vivo detection of applied electric currents by magnetic resonance imaging *Magn. Reson. Imag.* **7** 89-94

[40] Joy M L G, Lebedev V P and Gati J S 1999 Imaging of current density and current pathways in rabbit brain during transcranial electrostimulation *IEEE Trans. Biomed. Eng.* **46** 1139-49

[41] Khang H S, Lee B I, Oh S H, Woo E J, Lee S Y, Cho M H, Kwon O, Yoon J R and Seo J K 2002 J-substitution algorithm in magnetic resonance electrical impedance tomography

(MREIT): phantom experiments for static resistivity images *IEEE Trans. Med. Imag.* **21** 695-702

[42] Kerner T E, Paulsen K D, Hartov A, Soho S K, and Poplack S P 2002 Electrical impedance spectroscopy of the breast: clinical imaging results in 26 subjects *IEEE Trans. Med. Imag.* **21** 638-45

[43] Kim S W, Kwon O, Seo J K and Yoon J R 2002 On a nonlinear partial differential equation arising in magnetic resonance electrical impedance tomography *SIAM J. Math Anal.* **34** 511-26

[44] Kim Y J, Kwon O, Seo J K and Woo E J 2003 Uniqueness and convergence of conductivity image reconstruction in magnetic resonance electrical impedance tomography *Inv. Prob.* **19** 1213-25

[45] Kohn R and Vogelius M 1984 Determining conductivity by boundary measurements *Comm. Pure Appl. Math.* **37** 113-23

[46] Kwon O, Woo E J, Yoon J R and Seo J K 2002a Magnetic resonance electrical impedance tomography (MREIT): simulation study of J-substitution algorithm *IEEE Trans. Biomed. Eng.* **48** 160-7

[47] Kwon O, Lee J Y and Yoon J R 2002b Equipotential line method for magnetic resonance electrical impedance tomography (MREIT) *Inv. Prob.* **18** 1089-100

[48] Lee B I, Oh S H, Woo E J, Lee S Y, Cho M H, Kwon O, Seo J K and Baek W S 2003a Static resistivity image of a cubic saline phantom in magnetic resonance electrical impedance tomography (MREIT) *Physiol. Meas.* **24** 579-89

[49] Lee B I, Oh S H, Woo E J, Lee S Y, Cho M H, Kwon O, Seo J K, Lee J Y and Baek W S 2003b Three-dimensional forward solver and its performance analysis in magnetic resonance electrical impedance tomography (MREIT) using recessed electrodes *Phys. Med. Biol.* **48** 1971-86

[50] Metherall P 1998 Three Dimensional Electrical Impedance Tomography of the Human Thorax *University of Sheffield, Dept. of Med. Phys and Clin. Eng.*

[51] Mikac U, Demsar F, Beravs K and Sersa I 2001 Magnetic resonance imaging of alternating electric currents *Magn. Reson. Imag.* **19** 845-56

[52] Mosher J C, Leahy R M and Lewis P S 1999 EEG and MEG: forward solutions for inverse methods *IEEE Trans. Biomed. Eng.* **46** 245-59

[53] Nachman A 1988 A Reconstructions from boundary measurements *Ann. Math.* **128** 531-77

[54] Nachman A 1996 Global uniqueness for a two-dimensional inverse boundary value problem *Ann. Math.* **142** 71-96

[55] Oh S H, Lee B I, Woo E J, Lee S Y, Cho M H, Kwon O and Seo J K 2003 Conductivity and current density image reconstruction using harmonic B_z algorithm in magnetic resonance electrical impedance tomography *Phys. Med. Biol.* **48** 3101-16

[56] Oh S H, Lee B I, Lee S Y, Woo E J, Cho M H, Kwon O and Seo J K 2004 Magnetic resonance electrical impedance tomography: phantom experiments using a 3.0 Tesla MRI system *Mag. Reson. Med.* in press

[57] Park C, Park E J, Woo E J, Kwon O and Seo J K 2004a Static conductivity imaging using variational gradient B_z algorithm in magnetic resonance electrical impedance tomography *Physiol. Meas.* **25** 275-69

[58] Park C, Kwon O, Woo E J and Seo J K 2004b Electrical conductivity imaging using gradient B_z decomposition algorithm in magnetic resonance electrical impedance tomography (MREIT) *IEEE Trans. Med. Imag.* **23** 388-94

[59] Phillips J W, Leahy R M and Mosher J C 1997 MEG-based imaging of focal neuronal currents sources IEEE Med. Imag. **16** 338-48

[60] Polydorides N and Lionheart W R B 2002 A Matlab toolkit for three-dimensional electrical impedance tomography: a contribution to the electrical impedance and diffuse optical reconstruction software project *Meas. Sci. Technol.* **13** 1871-83

[61] Rank J B 1963 Specific impedance of rabbit cerebral cortex *Exp. Neurol.* **7** 144-52

[62] Saulnier G J, Blue R S, Newell J C, Isaacson D and Edic P M 2001 Electrical impedance tomography *IEEE Sig. Proc. Mag.* **18** 31-43

[63] Scott G C, Joy M L G, Armstrong R L and Henkelman R M 1991 Measurement of nonuniform current density by magnetic resonance *IEEE Trans. Med. Imag.* **10** 362-74

[64] Scott G C, Joy M L G, Armstrong R L and Hankelman R M 1992 Sensitivity of magnetic resonance current density imaging *J. of Magn. Reson.* **97** 235-254

[65] Scott G C 1993 *NMR Imaging of Current Density and Magnetic Fields* PhD Thesis, University of Toronto, Canada

[66] Seo J K, Kwon O, Lee B I and Woo E J 2003a Reconstruction of current density distributions in axially symmetric cylindrical sections using one component of magnetic flux density: computer simulation study *Physiol. Meas.* **24** 565-77

[67] Seo J K, Yoon J R, Woo E J and Kwon O 2003b Reconstruction of conductivity and current density images using only one component of magnetic field measurements *IEEE Trans. Biomed. Eng.* **50** 1121-4

[68] Seo J K, Kwon O, Ammari H, and Woo E J 2004a Mathematical framework and lesion estimation algorithm for breast cancer detection: electrical impedance technique using TS2000 configuration *IEEE Trans. Biomedical Eng.*

[69] Seo J K, Pyo H C, Kwon O, and Woo E J 2004b Image reconstruction of anisotropic conductivity tensor distribution in MREIT: computer simulation study *Physics in Medicine and Biology* **49** 4372-81

[70] Sersa I, Beravs K, Dodd N J F, Zhao S, Miklavcic D and Demsar F 1997 Electric current density imaging of mice tumors *Magn. Reson. Med.* **37** 404-9

[71] Silva J E, Marques J P and Jossinet J 2000 Classification of breast tissue by electrical impedance spectroscopy *Med. Biol. Eng. Comput.* **38** 26-30

[72] Sylvester J and Uhlmann G 1986 A uniqueness theorem for an inverse boundary value problem in electrical prospection *Comm. Pure Appl. Math.* **39** 91-112

[73] Sylvester J and Uhlmann G A 1987 global uniqueness theorem for an inverse boundary value problem *Ann. Math.* **125** 153-69

[74] Tidswell A T, Gibson A, Bayford R H and Holder D S 2001 Validation of a 3d reconstruction algorithm for EIT of human brain function in a realistic head-shaped tank. *NeuroImage* **13** 283-94

[75] Tidswell A T, Gibson A, Bayford R H and Holder D S 2001 Three-dimensional electrical impedance tomography of human brain activity. *Physiol. Meas.* **22** 177-86

[76] Uhlmann G 1999 Developments in inverse problems since Calderdon's foundational paper in *Harmonic Analysis and Partial Differential Equations* (Chicago, IL: Univ. Chicago Press) 295-345

[77] Van-Harreveld A and Schade J 1962 Changes in the electrical conductivity of cerebral cortex during seizure activity *Exp. Neurol.* **5** 383-400

[78] Webster J G ed. 1990 *Electrical Impedance Tomography* (Bristol, UK: Adam Hilger)

[79] Weinroth A P 1998 *Variable Frequency Current Density Imaging* MS Thesis, University of Toronto, Canada

[80] Woo E J, Lee S Y and Mun C W 1994 Impedance tomography using internal current density distribution measured by nuclear magnetic resonance *SPIE* **2299** 377-85

[81] Woo E J, Lee S Y, Seo J K, Kwon O, Oh S H and Lee B I 2004 Conductivity images of biological tissue phantoms using a 3.0 Tesla MREIT system *26th Ann. Int. Conf. IEEE EMBS* in press

[82] Yan R T H 1997 *Fast Radio-Frequency Current Density Imaging with Spiral Acquisition* MS Thesis, University of Toronto, Canada

[83] Yoon R 2000 *Characterization of Cortical Spreading Depression in Rat using Radio-Frequency Current Density Imaging* MS Thesis, University of Toronto, Canada

[84] Zhang N 1992 *Electrical Impedance Tomography based on Current Density Imaging* MS Thesis, Dept. of Elec. Eng., Univ. of Toronto, Toronto, Canada

Department of Mathematics, Yonsei University, Korea
Department of Mathematics, Konkuk University, Korea
College of Electronics and Information, Kyung Hee University, Korea